PAPER

Check for updates

N,Se co-doping strategy to boost the K⁺ storage performance of metal organic framework-derived 3D amorphous carbon

Yuyu Wang, [ID] * Liangqin Cai, Shuo Yuan, Lin Feng, Zhen Guo and Shihua Dong [ID] *

In view of cost-effectiveness, tunable interlayer spacing, and high electrical conductivity, carbonaceous materials are regarded as the most promising anodes for potassium-ion energy storage devices. Conversely, the poor diffusion kinetics, substantial volume changes caused by large-sized potassium ions (K⁺), and insufficient active sites limit the rate capability and cycling stability. Herein, a N,Se co-doped porous carbon octahedron (NSeC) material has been successfully synthesized by integrating microstructural engineering and surface-modification strategies, using UiO-66-NH₂ (a Zr-based MOF) as the precursor. The resultant NSeC featured a high content of edge N (pyrrolic N and pyridinic N) and abundant micropores, which ensured plentiful active sites and defects for K⁺ storage, thereby enhancing the diffusion kinetics of K⁺ and providing additional capacitive storage capacity. Accordingly, the NSeC anode displayed a high reversible capacity (228.8 mAh g⁻¹ at 0.5 A g⁻¹ after 1000 cycles), long cycling stability (195.6 mAh g⁻¹ at 2.0 A g⁻¹ over 3300 cycles) and excellent rate performance (158.4 mAh g⁻¹ at 10 A g⁻¹), which are superior to those of C and NC anodes. CV, charge/discharge curves and *in situ* Raman measurements were performed to reveal the high structural stability of the NSeC and its adsorption–intercalation mechanism for K⁺ storage. Moreover, the assembly of a full cell confirmed its potential for practical applications. This work could provide us with a greener, lower energy-consuming and more facile method for developing high-performance carbon-material anodes applicable to potassium-ion batteries.

Green foundation

1. This work advances green chemistry by adopting a facile MOF-induced strategy followed by post-treatment to fabricate N,Se co-doped carbon (NSeC) octahedral structures. The doping of Se atoms promotes the formation of edge N in the MOF-derived nitrogen-doped carbon materials to enhance the storage capacity of potassium ions, contributing to sustainability in energy storage.

2. The achieved NSeC features a high content of edge N (N-5 and N-6) and abundant micropores, and it shows fast potassium storage capabilities, promoted by a pseudocapacitive effect, enhanced kinetics and high structural stability.

3. Future work could develop high-performance carbon material anodes by modulating ligands of MOFs, achieving low cost and environmental sustainability, using green doping strategies, and this could be applicable to next-generation energy storage devices.

Introduction

Given the superiorities of abundant potassium resource, low redox potential (K/K⁺ = −2.93 V *vs.* standard hydrogen) and high cost-effectiveness, potassium-ion batteries (PIBs) with an analogous electrochemical storage mechanism to lithium-ion batteries have received widespread attention in the field of

large-scale renewable energy storage.[1–3] Anode material, as one of the components of PIBs, plays a crucial part in determining their properties. Thus, it is meaningful to explore appropriate K⁺ hosts, which can accommodate the larger radius of K⁺ (1.38 Å *vs.* 0.76 Å for Li⁺) and improve the sluggish kinetics and irreversibility of the intercalation.[4–7] Among the diverse anode candidates, including intercalation-type materials, metals, metal oxides, sulfides and selenides, carbonaceous nanostructures (especially amorphous carbons), stand out by virtue of their disordered structure, significant cost advantage, high structural stability and electrical conductivity. Nevertheless, the large radius of K⁺ and the limited intrinsic

Shandong Key Laboratory of Advanced Electrochemical Energy Storage Technologies, College of Energy Storage Technology, Shandong University of Science and Technology, Qingdao, Shandong 266590, People's Republic of China. E-mail: wangyy@sdust.edu.cn, dongsh@sdust.edu.cn

active sites of pure carbon materials make the de-/potassiation process more difficult, leading to inferior rate performance and restricted specific capacity.

Currently, microstructure engineering and surface modification strategies are widely employed to enhance the potassium storage performance of carbon materials. By constructing unique micro-nano structures, such as porous structures,[8–10] yolk–shell structures,[11–13] and hollow structures,[14–16] the diffusion paths of K^+ are shortened, active adsorption sites can be increased, and sufficient space can be provided to accommodate the volume changes during the insertion and extraction processes, thereby maintaining structural stability. In particular, the porous structure has a dual role in the potassium storage of the carbon anode, which can both contribute non-Faraday capacitance and facilitate the charge transfer.[17–19] Specifically, structures with different pore sizes have different functions in carbon anodes.[20–24] Micropores can enhance the non-Faraday capacitance capacity by increasing the specific surface area and providing additional potassium storage sites.[22] Mesopores serve as the main channel for ion diffusion and have a major role in facilitating the diffusion and enhancing the reaction kinetics,[23] whereas macropores can accelerate the penetration of the electrolyte.[24] For instance, Liang et al. successfully synthesized an "ideal" microporous anode material (NCS) for K^+ storage by constructing microporous structures, employing nitrogen-containing metal–organic frameworks (MOFs) as templates.[25] Mesoporous carbon nanowires with zinc-catalyzed short-range ordered structures were designed through a simple self-etching strategy for PIBs, demonstrating a high initial coulombic efficiency of 76.7% and excellent stability for 1000 cycles.[26] Accordingly, the potassium storage performance of the carbon anode with a porous structure can be significantly enhanced by providing additional active sites and accelerating the reaction kinetics.

Simultaneously, heteroatom doping, a representative surface-modification strategy, has been experimentally and theoretically shown to enhance the surface-induced capacitive storage capacity by introducing abundant active sites and defects in carbon materials.[27–29] Among the various heteroatoms (e.g., N, P, O, S, Se), nitrogen doping is one of the most extensively studied strategies, primarily due to the higher electronegativity of N atoms and their relative ease in forming chemical bonds with carbon.[30] Research has shown that nitrogen-doped carbon materials exhibit three main doping configurations: pyrrolic N (N-5), pyridinic N (N-6), and graphitic N (N-Q).[31,32] Among them, N-5 and N-6 are associated with surface-induced capacitive behavior, which can reduce the adsorption energy of K^+, while N-Q contributes to an increase in the electrical conductivity of the material. Therefore, nitrogen doping is beneficial for tuning the intrinsic characteristics of carbon materials. Compared with single nitrogen doping, co-doping strategies involving N with larger heteroatoms such as P and S have attracted widespread attention.[33,34] This is mainly due to the synergistic effects of co-doping, which intro-

duces more structural defects, voids, and edge sites for potassium storage, further expanding the interlayer spacing of carbon materials and facilitating ion insertion and extraction. In the case of N,S co-doped carbon, the introduction of S adjusts the nitrogen conformation in nitrogen-doped carbon materials and facilitates the conversion of N-Q to N-6 and N-5, whereas high contents of N-5 and N-6 create more defects and active sites, which can greatly enhance the K^+ storage capacity.[34] As a member of the sulfur group of elements, selenium shows potential as a co-doping element owing to its similar chemical properties to sulfur (similar electronegativity: 2.55 for Se and 2.58 for S) and its ability to undergo reversible reactions with K^+. Furthermore, Se has a larger atomic size and higher polarizability compared with S, which may impart unique performance advantages to Se-doped carbon materials.[35] Consequently, N,Se co-doped carbon materials are promising candidates as ideal anodes for K^+ storage. Generally, to obtain carbonaceous materials with a stable structure and excellent electrical conductivity, the synthesis requires high-temperature treatment (900–1600 °C, or even higher), which leads to high energy consumption and a relatively complex preparation process, violating the principles of "green" chemistry. Therefore, there is an urgent need to develop a more environmentally friendly, energy-efficient and simpler method to optimize the preparation process.

Herein, we successfully synthesized a three-dimensional (3D) porous NSeC through a facile MOFs-induced strategy followed by post-treatment, which integrated microstructure engineering and surface-modification strategies, employing UiO-66-NH$_2$ (Zr-based MOF) as the precursor. Compared with typical procedures, this work has significant features and the main differences, performances and green improvement are summarized in Table S1. First, the raw materials were relatively environmentally friendly and low-cost. Second, low-temperature pyrolysis at 700 °C consumed relatively low energy. Third, the introduction of selenium atoms in the carbonization process resulted in a simple material preparation process. Fourth, the as-prepared NSeC had excellent K^+ storage properties, reducing the frequency of electrode material replacement and the generation of waste. Specifically, the microporous-dominated porous structure could significantly increase the specific surface area, provide extra active sites and shorten ion-diffusion pathways. For N,Se co-doped carbon, N, Se co-doping not only increased the interlayer spacing and accelerated the diffusion of K^+ to a certain extent, it also favoured the enhancement of N-5 and N-6, forming more defects and active sites, and thus promoting the K^+ storage capacity. Consequently, the NSeC anode delivered high reversible capacity, excellent rate capability and stable cycling behavior due to a synergistic contribution of heteroatom doping and microporous structure, which were clarified by kinetic analysis and in situ Raman spectroscopy. More importantly, when coupled with a $K_{1.64}Fe[Fe(CN)_6]_{0.89} \cdot 0.15H_2O$ cathode for a full cell, it also achieved good cycling stability with a satisfactory capacity of 108.4 mAh g^{-1} at 0.5 A g^{-1} after 200 cycles, which showed its potential application for potassium-ion storage.

Experimental

Preparation of UiO-66-NH$_2$ and UiO-66 precursors

The regular UiO-66-NH$_2$ polyhedra were fabricated based on the reported experimental conditions[36] with further modification. First, ZrCl$_4$ powder (1.7 mmol) was dissolved in 75 mL of N,N-dimethylformamide (DMF) with the assistance of ultrasound at 55 °C. Then, 2.85 mL of acetic acid was added into the above solution. After that, a DMF solution of 2-aminoterephthalic acid (1.7 mmol in 25 mL of DMF) was poured in, followed by addition of deionized water (0.125 mL) at 60 °C. The mixture was sonicated for a few minutes and placed in an oil bath at 120 °C for 24 h. After centrifugation and washing thrice with ethanol, the UiO-66-NH$_2$ precipitate was collected. For UiO-66 precursors, the preparation procedure was highly consistent with that for UiO-66-NH$_2$, using terephthalic acid instead of 2-amino-terephthalic acid as the organic ligand.

Synthesis of N,Se-co-doped carbon (NSeC), N-doped carbon (NC) and C octahedral frameworks

The as-prepared UiO-66-NH$_2$ powder and selenium powder with a mass ratio of 1 : 2 were, respectively, placed in two crucibles and heated to 700 °C at a heating rate of 2 °C min^{-1} and kept for 2 h in H$_2$/Ar (5% H$_2$). Then, the sample was etched by 20 wt% hydrofluoric acid (HF) at 80 °C overnight and washed to neutral pH with deionized water and dried, obtaining the N, Se–C octahedra.

For the preparation of NC, UiO-66-NH$_2$ was directly calcined in a tubular furnace without adding selenium powder, and the other condition was the same as for NSeC. C could be fabricated by direct high-temperature pyrolysis of UiO-66 precursors and the subsequent acid-etching procedure.

Material characterization

The morphologies and microstructure of the above samples were characterized using a scanning electron microscope (5.0 kV, Regulus 8100, Hitachi) and a high-resolution transmission electron microscope (200 kV, Talos F200s, FEI) with energy-dispersive X-ray spectroscopy (EDS) using the Super-X detection system. X-ray diffraction (XRD) patterns were collected with a X'Pert Pro MPD (λ = 1.5418 Å) system. Raman spectroscopy was carried out on a Labram HR Evolution spectroscope (HORIBA) using an excitation wavelength of 532 nm as the laser light source. Electron paramagnetic resonance (EPR) spectroscopy was carried out on a EMXplus-9.5/12 spectrometer (Bruker). X-ray photoelectron spectroscopy (XPS) was employed to characterize the surface chemical states of samples using an ESCALAB XI+ analyzer (Thermo Scientific). N$_2$ adsorption–desorption curves were obtained using a Micro ASAP2020 gas sorption analyzer. The pore-size distribution was analyzed by the Barrett–Joyner–Halenda (BJH) method.

Electrochemical measurements

The CR2032 coin cells with potassium metal as the counter electrode were assembled in a glove box under 99.999% argon atmosphere to evaluate the electrochemical performance. For the working electrode, the as-prepared active material (60 wt%), carbon black conductive agent (ECP600JD, 20 wt%) and sodium carboxymethyl cellulose binder (20 wt%) were dispersed in deionized water and coated on copper foil. Then, a KFSI solution (1.0 mol L^{-1}) dissolved in ethylene carbonate/dimethyl carbonate (1 : 1 in volume) and Whatman glass fiber (GF/A) were employed as the electrolyte and separator, respectively. Cyclic voltammetry (CV; 0.01–3.0 V, 0.1–1.0 mV s^{-1}) curves and electrochemical impedance spectroscopy (EIS; 10^5–0.1 Hz) profiles were collected on a Gamry 30115 electrochemical workstation. To record galvanostatic charge/discharge cycling at various current densities and the galvanostatic intermittent titration technique (GITT; a current pulse of 50 mA g^{-1} for 10 min, followed by rest for 60 min) curves, Neware-5 V 10/20 mA battery systems (Shenzhen Xinwei) were utilized at room temperature. The diffusion coefficient of K$^+$ (D_K) was calculated by the equation:[24,36]

$$D_K = \frac{4}{\pi\tau}\left(\frac{m_A V_M}{M_A S}\right)^2 \left(\frac{\Delta E_s}{\Delta E_\tau}\right)^2$$

where the duration of the current impulse and geometric area of the electrode are marked as τ and S, respectively. M_A, m_A, V_m stand for the molar weight, active mass, molar volume of the carbon material, respectively. ΔE_s represents the equilibrium potential difference before and after the current pulse, ΔE_τ signifies the potential variation during the current pulse.

As for full cells, the cathode was composed of homemade K$_{1.64}$Fe[Fe(CN)$_6$]$_{0.89}$·0.15H$_2$O (K-FeHCFe),[37] carbon black and poly(vinylidene fluoride) (PVDF) with the weight ratio of 8 : 1 : 1 in N-methyl-2-pyrrolidone (NMP). Before assembly, the K-FeHCFe cathode and NSeC anode were first cycled in half-cells for two cycles at 0.05 A g^{-1}. The electrochemical performance of full cells was measured in a voltage range of 0.5–3.2 V.

Results and discussion

Fig. 1a depicts the step-by-step synthesis of the NSeC octahedron. Specifically, the UiO-66-NH$_2$ precursor with structural defects was prepared by a solvothermal reaction using nitrogen-containing 2-aminoterephthalic acid as the organic ligand. Following high-temperature selenization at 700 °C, the coordinated zirconium salts and 2-aminoterephthalic acid ligands transformed into ZrO$_2$ and N doped carbon (NC), respectively. Additionally, Se species were simultaneously introduced into NC layers to form N,Se co-doped carbon (NSeC) during selenization, resulting in ZrO$_2$ nanoparticles embedded in N,Se co-doped carbon octahedral frameworks (denominated as ZrO$_2$/NSeC, Fig. S1). Subsequently, HF acid was adopted to remove the inactive potassium storage component (ZrO$_2$), aiming to generate NSeC polyhedral structures with a porous structure. Scanning electron microscopy (SEM) revealed that the UiO-66-NH$_2$ precursor had a homogeneous octahedral structure with a smooth surface (Fig. 1b). After thermal treatment and etching, polyhedral structures similar to that of the precursor were observed in NC (Fig. S2a and S2b)
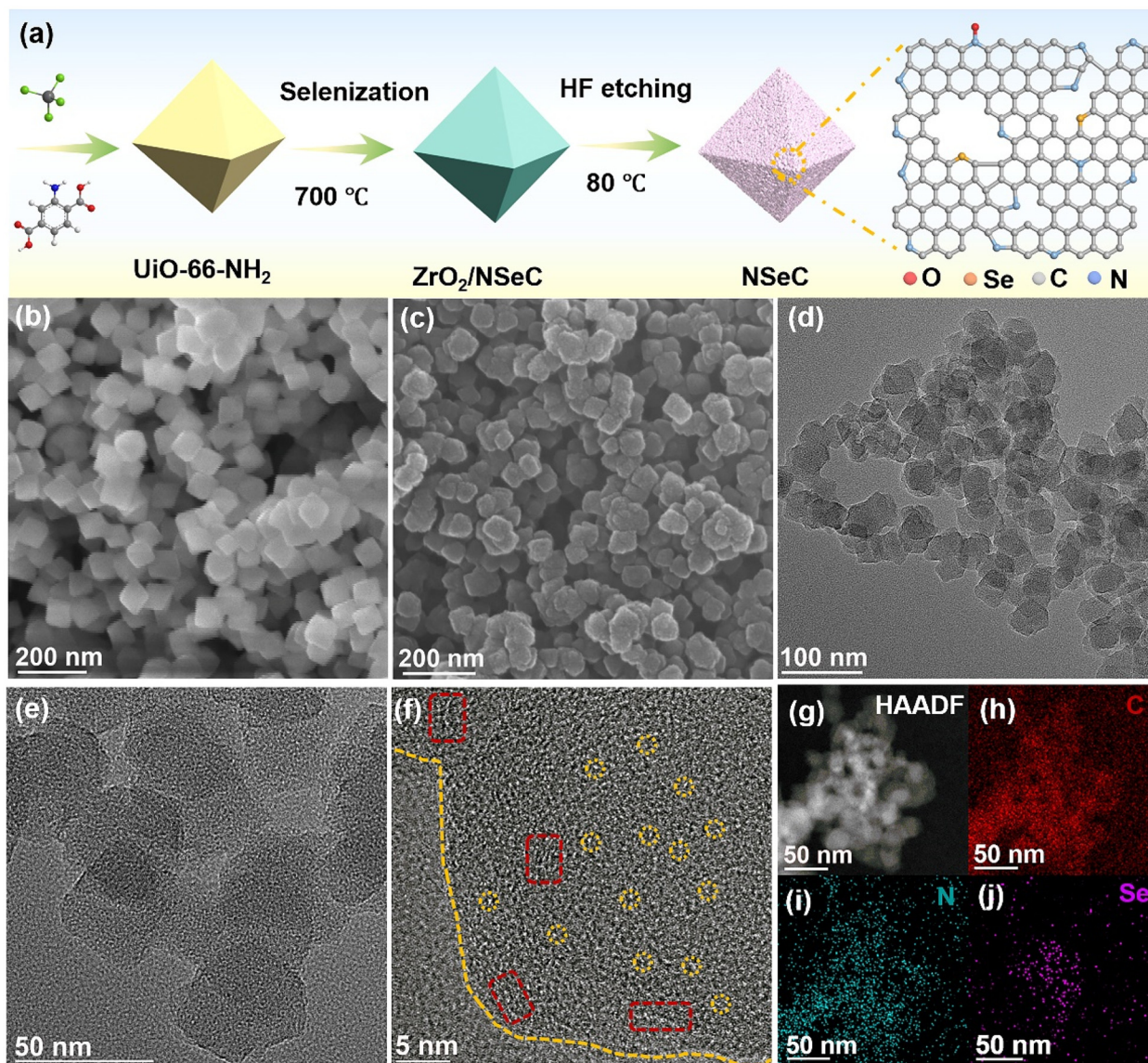
Fig. 1 (a) A schematic illustration of the synthesis of NSeC. SEM images of (b) UiO-66-NH$_2$ and (c) NSeC. (d and e) TEM images, (f) a HRTEM image, (g) a HAADF image and the corresponding EDX elemental mapping of (h) C, (i) N and (j) Se in NSeC.

and NSeC (Fig. 1c) except for the rough surface, indicating the high stability of the precursor. In the UiO-66-NH$_2$ structure, Zr(IV) ions and carboxylic acid ligands are regarded as hard acid and hard base, respectively.[38] The strong coordination bond between them endows the precursor with excellent stability, which ensures that it can maintain the integrity of the polyhedral structure even after subsequent high-temperature heating and etching. Similarly, C derived from the UiO-66 precursor exhibited undamaged polyhedron morphology (Fig. S2c and S2d). The uniform octahedrons of NSeC with intact structures were further confirmed by transmission electron microscopy (TEM), as displayed in Fig. 1d and e. Meanwhile, the high-resolution TEM (HRTEM) image in Fig. 1f showed many short-range ordered regions (dotted red boxes) in NSeC, verifying its amorphous feature. Besides, abundant pores

(yellow circled areas) could be detected, which may provide more favourable conditions for K$^+$ storage. As visualized in the high-angle annular dark field (HAADF) image (Fig. 1g) and elemental mapping images (Fig. 1h–j), the elements of N,Se, and C were recorded in the octahedral structure, further confirming the doping of N and Se throughout the carbon.

The XRD patterns of C, NC and NSeC are presented in Fig. 2a. All three samples had a broad diffraction peak at ~25° associated with the (002) plane of amorphous carbonaceous materials,[39,40] which was consistent with TEM observations. Interestingly, the (002) plane of NSeC shifted slightly towards a lower angle, suggesting that the doping of selenium had increased the disorder and defective character of the material to some extent. This was confirmed in the Raman and EPR results. The Raman spectra (Fig. 2b and Fig. S3) showed
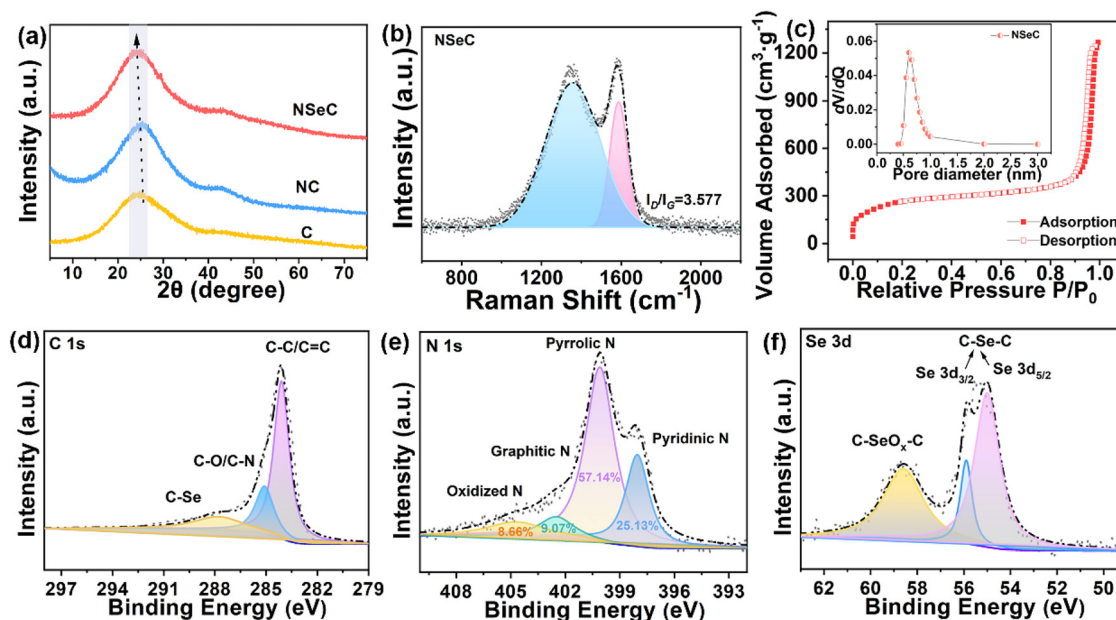
Fig. 2 Composition and structural characterization of carbon materials. (a) XRD patterns, (b) the Raman spectrum, (c) the N_2 adsorption/desorption isotherm and corresponding pore-size distribution curve, and high-resolution (d) C 1s, (e) N 1s, and (f) Se 3d XPS spectra for NSeC.

characteristic peaks at ≈1340 cm^{-1} for the D-band and 1590 cm^{-1} for the G-band in three carbon materials, originating from the defected and disordered carbon and the stretching vibrations of sp^2 hybridized carbon, respectively.[21] The calculated ratio (I_D/I_G) for C, NC, and NSeC was 3.173, 3.394, and 3.577, respectively. As shown in Fig. S4, NSeC and NC exhibited EPR signals at $g = 2.003$, corresponding to unpaired electrons on π-conjugated carbon atoms,[41] indicating the formation of carbon vacancies. Moreover, compared with C and NC, NSeC exhibited a stronger peak intensity, suggesting a higher concentration of edge defects in NSeC. The higher I_D/I_G and stronger peak intensity of the EPR signal for NSeC implied that more defects and disorders had been introduced after nitrogen and selenium co-doping, which could offer more active sites for K$^+$ storage. Moreover, the N_2 adsorption–desorption measurement was used to verify the porous property of NSeC. In Fig. 2c, the adsorption curves of the NSeC exhibited typical I-type isotherm characteristics with a high BET specific surface area of 942.1 m^2 g^{-1}, which indicated that its pore structure was dominated by micropores (pore size <2 nm). Combined with the data for pore-size distribution (concentrated at 0.5–1.0 nm), the dominance of micropores in NSeC could be further confirmed. It not only increased the specific surface area, it also improved the wettability of the electrolyte, thereby enhancing the storage capacity of K$^+$. In addition, XPS spectra gave detailed information about the surface chemical states and elemental composition of NSeC. From the survey spectrum (Fig. S5), the elements of N, Se and C could be detected, indicating that N and Se were doped into the 3D carbon framework. Fig. 2d presents the high-resolution C 1s spectrum, which could be deconvoluted into the dominant C–C/C=C peak at 284.1 eV, along with the C–N/C–O peak at

285.1 eV, and the C–Se peak at 287.9 eV.[27,42] The fitted N 1s spectrum is displayed in Fig. 2e, where distinct peaks at 398.1, 400.1, 402.6 and 404.8 eV were attributed to the pyrrolic N, pyridinic N, graphitic N, and oxidized N, respectively.[43] Notably, the contents of pyrrolic N (57.14%) and pyridinic N (25.13%) were significantly higher than those of graphitic N (9.07%) and oxidized N (8.66%). This effect may have originated from the increase in the number of defect sites after Se doping, thus making NSeC exhibit more surface-induced capacitive behavior and rapid ion transport kinetics.[27,44] In the high-resolution spectrum of Se 3d (Fig. 2d), peaks at 55.0 and 55.9 eV were depicted, belonging to Se $3d_{5/2}$ and Se $3d_{3/2}$ in –C–Se–C– covalent bonds; the peak at 58.6 eV was related to the oxidized –Se group (C-SeO$_x$-C).[45] Therefore, the formation of C–Se, C–N, and C–Se–C bonds further indicated the construction of nitrogen and selenium co-doped carbon, which implied more active sites in NSeC to boost its potassium storage performance.

Afterwards, three types of carbon anodes and potassium metal were assembled into half-cells to estimate their potential storage performance. The CV curves of NSeC at a scan rate of 0.1 mV s^{-1} with a potential window range of 0.01–3.0 V are shown in Fig. 3a. During the first cycle, an irreversible cathodic peak appeared around 0.50 V and disappeared in subsequent scans, which may have been related to the formation of the solid electrolyte interphase (SEI) film and the decomposition of the electrolyte.[46] Besides, one pair of reduction/oxidation peaks at ~0.01/0.3 V were observed, representing the intercalation/de-intercalation of K$^+$ between NSeC layers.[47] Profiles except for the first cycle showed a high degree of agreement with no significant variation, which suggested excellent reversibility of the NSeC electrode. Specifically, compared with
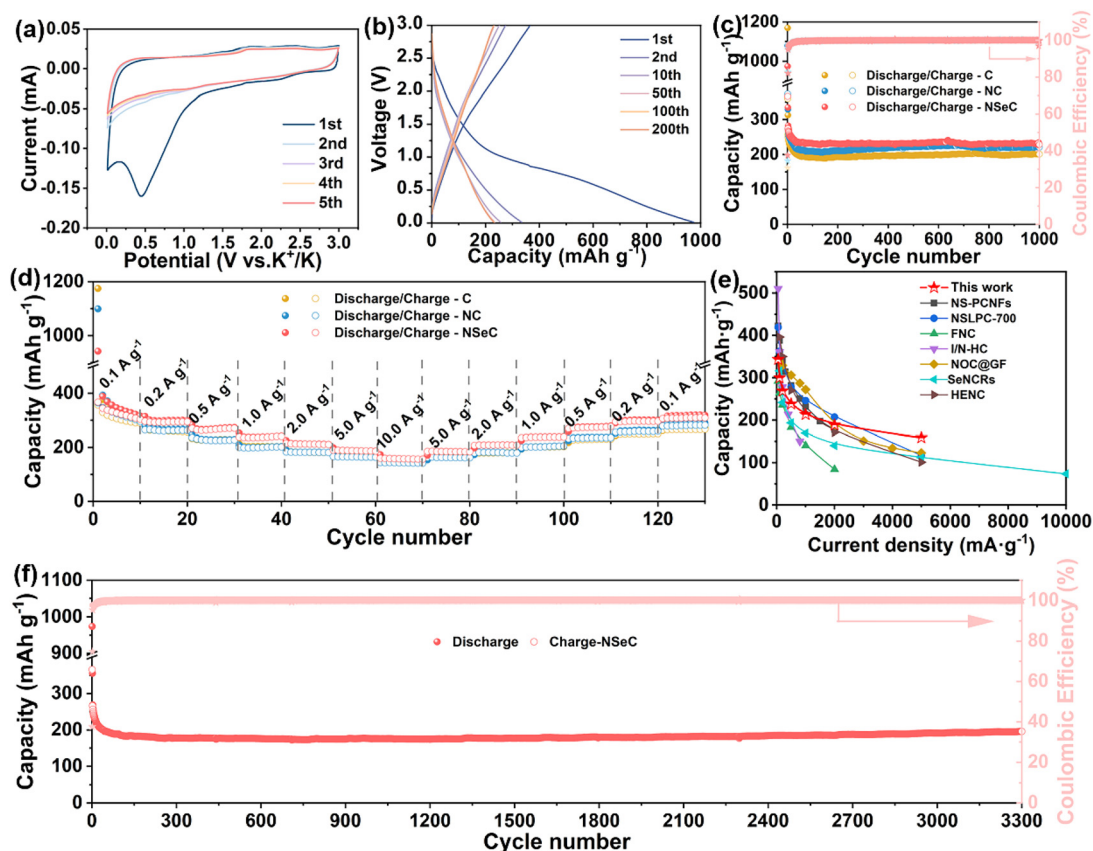
Fig. 3 K$^+$ storage performance of carbon-material anodes in half-cells. (a) Initial five CV curves at 0.1 mV s^{-1} and (b) selected galvanostatic discharge/charge profiles of NSeC. (c) Cycling stability at 0.5 A g^{-1} and (d) rate capability at different current densities from 0.1 to 10.0 A g^{-1} for C, NC and NSeC. (e) A comparison of rate capability for NSeC and other reported heteroatom-doped carbon-material anodes. (f) Long-term cycling performance of NSeC at a high current density of 2.0 A g^{-1}.

the CV results of C and NC (Fig. S6), there was an extra anodic peak of 1.8 V for NSeC, corresponding to the reaction process of the K ion on the active site induced by Se doping.[48] Similar CV curves implied the same potassium storage mechanism. Differently, NSeC exhibited a lower K$^+$ intercalation *plateau* compared with NC, as described in differential capacity (dQ/dV) curves (Fig. S7). This finding indicated that its capacity contribution was dominated at lower potentials compared with NC, which is beneficial for enhancing the energy density of PIBs. From the selected charge/discharge curves of NSeC at 0.5 A g^{-1} in Fig. 3b, a typical slope characteristic in the high region was recorded, demonstrating that the adsorption reaction (surface-induced capacitive behavior) dominated the storage of K$^+$ owing to a substantial number of defects in NSeC. Also, it showed the first discharge/charge capacities of 973.9/365.9 mAh g^{-1}, giving an initial coulombic efficiency (ICE) of 37.6%, which is comparable to (or even higher than) previously reported values (Table S2). The relatively low ICE is a common phenomenon for carbon-based materials in PIBs, which could be associated with the irreversible electrolyte decomposition, low reversibility of potassiation/depotassiation, high specific surface area and porosity, as well as defect/surface functional group trapping.[49,50] Strategies such as

carbon surface/structure optimization, electrolyte engineering, binder modification and pre-anodization can be employed to address the low ICE of carbon-based anodes.[50] Intriguingly, the ICE of NSeC and NC (34.6%) (Fig. S8b) was higher than that of the C electrode (30.7%, Fig. S8a), which suggested that heteroatom doping could alleviate electrolyte decomposition to some extent.[49] After the first cycle, the Coulomb efficiency (CE) of the second cycle was improved to 82%, and up to 99% could be reached at 50 cycles. The charging/discharge profiles of 50th, 100th and 200th cycles with similar trends and shapes once again suggested the high stability of NSeC. Furthermore, to verify the superiority of heteroatom co-doping in potassium storage performance, the cyclic stability and rate capacity of the three samples were systematically compared. As illustrated in Fig. 3c, due to abundant defects and active sites, the NSeC electrode provided stable charge/discharge capacities of 228.2/228.8 mAh g^{-1} after 1000 cycles at 0.5 A g^{-1}, with a CE as high as 99.7%. Even at a large current density of 2.0 A g^{-1}, a highly reversible specific capacity of 195.6 mAh g^{-1} after 3300 cycles was maintained (Fig. 3f), demonstrating its excellent cycling stability. In contrast, for the C electrode, only 201 mAh g^{-1} could be exhibited at the 1000th cycle under a current density of 0.5 A g^{-1}, which was lower than that of the NSeC electrode.

The same results are displayed in Fig. 3d. The capacity of the NSeC electrode decreased as the current density increased from 0.1, 0.2, 0.5, 1.0, 2.0, and 5.0, to 10.0 A g^{-1}, exhibiting an average specific capacity of 343.1, 299.4, 268.3, 237.8, 212.9, 188.3, and 158.4 mAh g^{-1}, respectively. In addition, when the current density was gradually reduced from 10.0 A g^{-1} back to 0.1 A g^{-1}, the specific capacity of NSeC recovered to its initial level, demonstrating excellent reversibility and rate performance, which was superior to the C, NC electrodes and some other reported heteroatom-doped carbon materials (Fig. 3e).[42,51–56] The excellent potassium storage performance of NSeC electrodes could be attributed to the synergistic doping effect of nitrogen and selenium as well as the advantages of a porous structure. On the one hand, selenium doping could increase the interlayer spacing of carbon materials and also increase the content of edge N (N-6 and N-5), which not only promoted the adsorption of K$^+$ but also introduced a large number of ion storage defect sites. On the other hand, the rapid diffusion and intercalation/deintercalation of K$^+$ could be promoted in the porous structure, thereby significantly enhancing the storage capacity and reaction kinetics performance.

CV, EIS and GITT measurements were applied to further analyze the potassium storage kinetic features of three carbon anodes. As shown in Fig. 4a and Fig. S9, the shapes of CV curves for the three samples remained almost identical and exhibited a similar tendency to become larger with increasing scanning rate, indicating the surface-controlled (capacitive-like reaction) processes for potassium-storage capacity.[57] Typically, the b value reflects the main storage mechanism, which can be acquired through the relationship between the peak current (i) and scan rate (v).[21,24,54] If b is 0.5, a diffusion-controlled dominated storage process can be present, while the surface

pseudocapacitive behavior is dominant if b approaches 1.0. The b values of C, NC, and NSeC were calculated from the fitting lines in Fig. 4b, giving 0.841, 0.863 and 0.873 for the cathodic process and 0.885, 0.882 and 0.892 for the anodic process, respectively. The high b values demonstrated that the pseudocapacitance behavior had a major role in K$^+$ storage capacity. Moreover, the equation $i(V) = k_1 v + k_2 v^{1/2}$ was employed to quantify the contribution of capacitive behavior.[21,24,54] Fig. 4c provides the detailed capacitive contributions for the three electrodes at scan rates of 0.2, 0.4, 0.6, 0.8 and 1.0 mV s^{-1}. For the NSeC electrode, the surface capacitance contribution increased from the initial 58.1% to 75.7% at 1.0 mV s^{-1} (Fig. S10). Apparently, among these carbon electrodes, NSeC had the highest pseudocapacitive area contribution ratio at all tested scan rates. This may have been closely related to the active sites introduced by N/Se co-doping in the NSeC material, porous structure, and the increased content of edge N (N-6 and N-5). These features would have endowed NSeC with capacitive behavior, facilitating enhancement of the surface reactivity of the electrode and promoting the rapid adsorption/desorption of K$^+$. The fast reaction kinetics were further supported by EIS and GITT results. As plotted in Fig. S11a and S11c, the Nyquist plots of three samples before and after cycling were all composed of a semicircle in the high-frequency region and a sloping line in the low-frequency region, corresponding to the charge transfer resistance (R_{ct}) and the ionic diffusion capability, respectively.[53] For the electrode before cycling, NSeC exhibited the smallest R_{ct} (1087 Ω) compared with that of C (1288 Ω) and NC (1199 Ω). And the same results could be clearly observed after cycling (Fig. S11c), confirming the superior electrical conductivity of NSeC. Besides, for the Bode plots (inset in Fig. S11a and S11c), the NSeC electrode before and after cycling exhibited a smaller
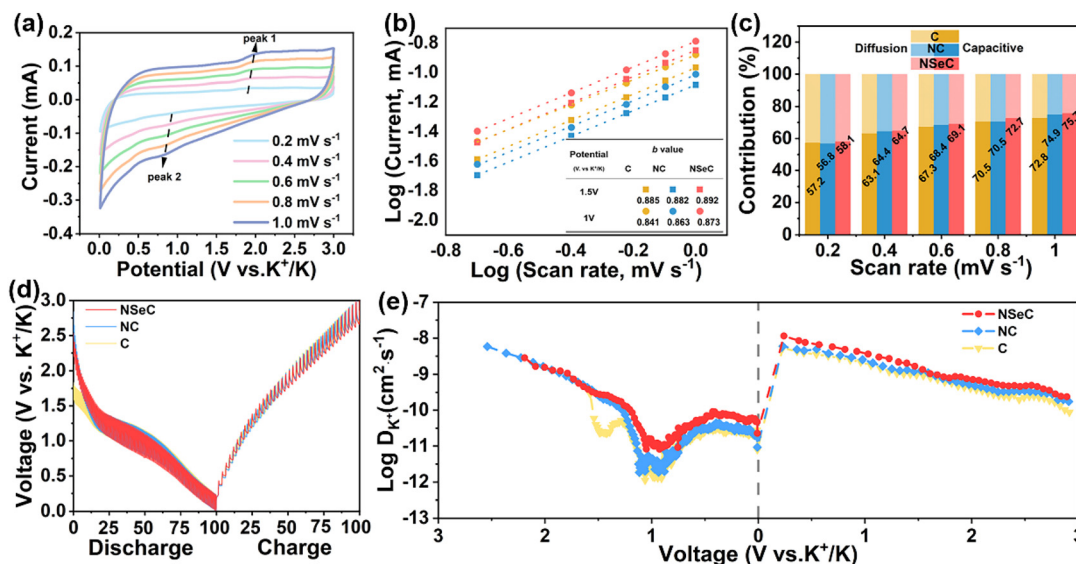

Fig. 4 Kinetics analysis for K$^+$ storage. (a) CV curves of NSeC at various scan rates from 0.2 to 1.0 mV s^{-1}. (b) Calculated b values, (c) the contribution ratios of capacitive and diffusion-controlled capacities at different scan rates, (d) GITT profiles during the first potassiation/depotassiation and (e) corresponding K$^+$ diffusion coefficients of C, NC and NSeC.

phase angle in the low-frequency region, indicating its faster ion diffusion rate. Furthermore, the K^+ diffusion capabilities of the three samples could be qualitatively compared by equation: $D_k = R^2T^2/2A^2n^4F^4C^2\sigma^2$.[42] When the measured parameters were fixed, a smaller Warburg factor (σ value, the slope of the line relating the real impedance (Z') to $\omega^{-1/2}$ in the low-frequency region) corresponded to a faster K^+ diffusion rate. From Fig. S11b and Fig. S11d, the smallest σ value of NSeC before and after cycling could be calculated compared with those of NC and C, demonstrating its superior K^+ storage kinetics. According to GITT profiles (Fig. 4d), the three electrodes had similar trends, which was in good agreement with the charge/discharge curves. Based on Fick's second law,[43] the D_k values were recorded and calculated in Fig. 4e and Table S3. The NSeC electrode displayed higher D_k values ($10^{-11.0854}$ to $10^{-7.93634}$) compared with the D_k values of C ($10^{-11.9531}$ to $10^{-8.27452}$) and NC ($10^{-11.7362}$ to $10^{-8.22348}$) upon potassiation and depotassiation. These data suggested that the faster reaction kinetics for the NSeC electrode may be attributed to enlarged interlayer spacing, abundant edge N active sites (high content of pyrrolic N (57.14%) and pyridinic N (25.13%)) and a porous structure.

To reveal the possible reasons for its excellent electrochemical properties, *in situ* Raman spectroscopy was performed to gain insights into the electrochemical reaction mechanism of the NSeC electrode during potassiation/depotassiation. A series of representative *in situ* Raman spectra collected during the charging and discharging process are exhibited in Fig. 5a, which recorded the structural evolution (peak positions and intensities of D and G bands) of the carbon material. Specifically, the D band was not significantly shifted during potassiation/depotassiation, but its peak intensity gradually weakened as discharging proceeded, which may have been due to the interaction between the defect structures (*e.g.*,

vacancies and edge sites) in the carbon material and K^+. In contrast, the G band shifted to lower wavenumbers during discharge and its intensity also gradually decreased. These effects could be attributed to the occupation of electrons in the $\pi^\star$ antibonding band and the weakening of C–C bonds caused by the continuous intercalation of K^+ in the short-range ordered graphite domains.[58] Strikingly, during subsequent charging, the D band and G band gradually recovered to their original states, revealing the excellent structural stability and electrochemical reversibility of the NSeC anode during K^+ insertion/extraction. In addition, this structural stability was confirmed by the morphology of the NSeC electrode after 100 cycles, as shown in Fig. S12, revealing the integrity of the octahedral structure. To visualize the dynamic changes of D and G bands during charging and discharging, we plotted the contour plots of the Raman spectra, as presented in Fig. 5b. As discharging proceeded, the intensity of the D and G peaks showed a weakening tendency, which confirmed the adsorption of K^+ on active sites and their insertion into carbon layers.[49,59] Combined with the results of *in situ* Raman spectroscopy, CV and charge/discharge curves, the potassium storage process of NSeC could be classified as an "adsorption–intercalation" mechanism (Fig. 5c). The latter could be divided into two stages: (i) adsorption of K^+ at the active site of the surface or defect, corresponding to the high potential platform region capacity; (ii) insertion of K^+ into the carbon layer, which was attributed to the capacity for the low potential platform region.

To evaluate the potassium storage capability of NSeC for practical application, full cells were assembled using activated NSeC as the anode and homemade K-FeHCFe as the cathode (Fig. 6a). The well-defined crystallinity and phase purity in the XRD pattern (Fig. S13) indicated preparation of the K-FeHCFe cathode. For the K-FeHCFe//K half-cell, as described in Fig. 6b, the charging and discharging curves were highly coincident
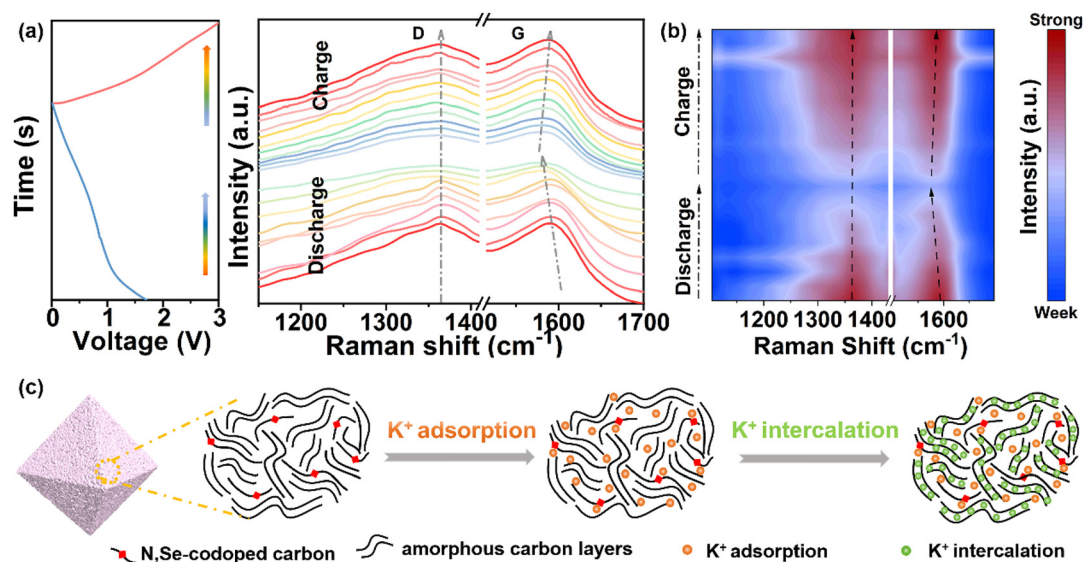

Fig. 5 Investigation of the K^+ storage mechanism in NSeC. (a) *In situ* Raman spectra and (b) a contour plot of *in situ* Raman data for the NSeC electrode during the first charge/discharge. (c) A schematic diagram depicting the potassium storage mechanism for NSeC.
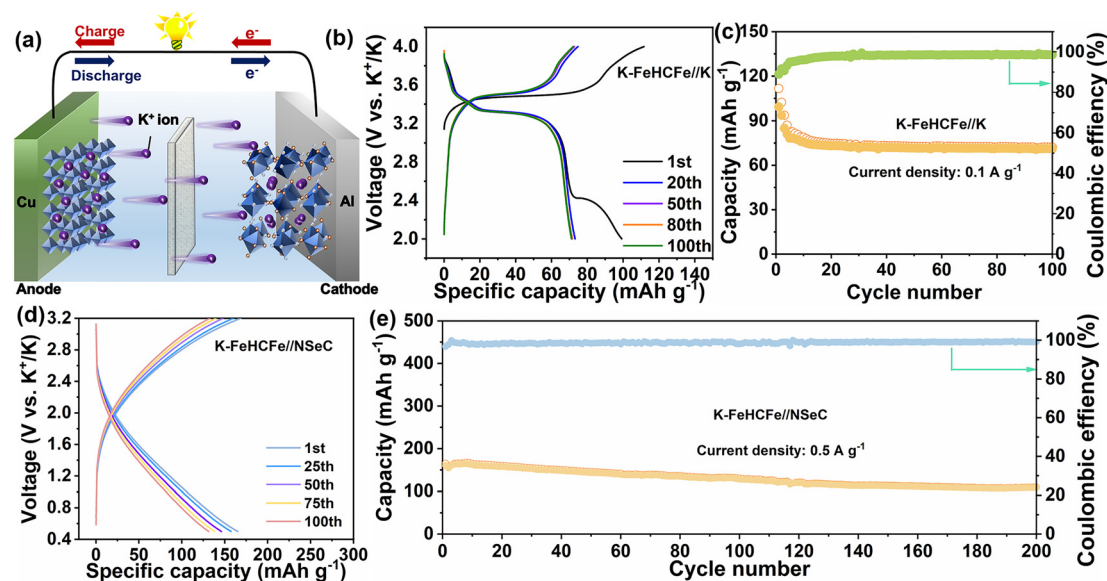
Fig. 6 (a) A schematic illustration of the K$^+$ full cell. (b) Galvanostatic charge/discharge curves and (c) cycling performance at 0.1 A g^{-1} for the K-FeHCFe//K half-cell. (d) Charge/discharge profiles of the K-FeHCFe//NSeC full cell between 0.5 V and 3.2 V and (e) its long-term cycling performance at 0.5 A g^{-1}.

from 20th to 100th cycles, suggesting its excellent cycling stability. This could also be confirmed by the cycling performance (Fig. 6c): a stable discharge capacity of 71.2 mAh g^{-1} could be maintained after 100 cycles at 0.1 A g^{-1}. Subsequently, the K-FeHCFe//NSeC full cells were measured with the working voltage range 0.5–3.2 V. From Fig. 6d, a similar varying trend of selected charge/discharge curves for the full cell could be observed, exhibiting its high reversibility. Even after 200 cycles at 0.5 A g^{-1}, an expected charge/discharge capacity of 109.3/108.4 mAh g^{-1} could be delivered (based on the anode mass), giving an excepted CE of 99.2%. This homemade NSeC//K-FeHCFe full cell has certain advantages in terms of specific capacity and cycling stability compared with the literature (Table S4), which further validated its potential for practical applications in PIBs and provided important insights for the development of next-generation high-performance energy storage devices.

number of defective vacancies, which significantly enhanced the adsorption and storage capacities of K$^+$ (high capacities of 228.2/228.8 mAh g^{-1} after 1000 cycles at 0.5 A g^{-1}). Simultaneously, the existence of the porous structure effectively promoted the rapid transport of K$^+$, thus ensuring excellent rate performance (158.4 mAh g^{-1} at 10 A g^{-1}) and long-term cycling stability (desired reversible specific capacity of 195.6 mAh g^{-1} after 3300 cycles at a high current density of 2.0 A g^{-1}). *In situ* Raman spectroscopy demonstrated the high structural stability and electrochemical reversibility of NSeC during repeated de/intercalation, and its adsorption–intercalation mechanism for potassium storage was also confirmed. In addition, a full cell assembled with the NSeC anode and K-FeHCFe cathode (K-FeHCFe//NSeC) delivered a high reversible specific capacity and cycling stability, further demonstrating that NSeC is one of the most promising anode candidates for high-performance PIBs.

Conclusions

In general, a facile MOF-induced strategy followed by post-treatment was adopted to fabricate a N,Se co-doped carbon octahedral structure. Through the introduction of selenium heteroatoms and subsequent etching treatment, NSeC octahedra with more N-doping sites and abundant microstructure could be achieved, which are beneficial for the storage of K$^+$, including a higher potassium storage capacity as well as faster potassium storage kinetics. Specifically, the doping of selenium atoms adjusted the nitrogen configuration in the nitrogen-doped carbon materials and promoted the formation of N-6 and N-5. This high content of N-6 and N-5 induced a large

Author contributions

Yuyu Wang: experiment design, material synthesis, electrochemical performance measurements, data collection/analyses, manuscript revision/writing. Liangqin Cai: data analyses and writing the original manuscript. Shuo Yuan: data analyses and investigation. Lin Feng: data analyses. Zhen Guo: methodology. Shihua Dong: manuscript reviewing and editing. All authors approved the final version of this manuscript.

Conflicts of interest

There are no conflicts of interest to declare.

Data availability

The data supporting this article have been included as part of the SI: Fig. S1–S13 and Tables S1–S4. See DOI: **https://doi.org/10.1039/d5gc01554e**.

Acknowledgements

References

1 J. Ge, L. Fan, A. M. Rao, J. Zhou and B. Lu, *Nat. Sustain.*, 2022, **5**, 225–234.

2 D. Xu, L. Chen, X. Su, H. Jiang, C. Lian, H. Liu, L. Chen, Y. Hu, H. Jiang and C. Li, *Adv. Funct. Mater.*, 2022, **32**, 2110223.

3 S. Dhir, B. Jagger, A. Maguire and M. Pasta, *Nat. Commun.*, 2023, **14**, 3833.

4 X. Zhu, F. Xia, D. Liu, X. Xiang, J. Wu, J. Lei, J. Li, D. Qu and J. Liu, *Adv. Funct. Mater.*, 2023, **33**, 2207548.

5 S. Chen, J. Zhong, H. Deng, Q. Wei, X. Shen, X. Jia, S. Li, Q. Zhang, J. Zhu, B. Lu and W. Yang, *CCS Chem.*, 2024, **6**, 1011–1023.

6 M. Ma, S. Chong, K. Yao, H. K. Liu, S. X. Dou and W. Huang, *Matter*, 2023, **6**, 3220–3273.

7 X. Liu, J.-H. Chu, Z.-X. Wang, S.-W. Hu, Z.-Y. Cheng, K.-N. Liu, C.-J. Zhang, L.-Q. Zhang, L.-D. Xing and W. Wang, *Rare Met.*, 2024, **43**, 5516–5548.

8 Y. S. Zhou, Y. C. Zhu, Y. Liu and B. S. Xu, *Small*, 2024, **21**, 2408974.

9 C.-C. Wang, S.-E. Tseng and H. M. Wang, *J. Energy Storage*, 2024, **89**, 111631.

10 Q. Ren, L. Yan, X. Yu, W. Lei, Z. Sun, R. Hao, J. Yang and Z. Shi, *Chem. Eng. J.*, 2024, **499**, 156271.

11 F. Yang, H. Gao, J. Hao, S. Zhang, P. Li, Y. Liu, J. Chen and Z. Guo, *Adv. Funct. Mater.*, 2019, **29**, 1808291.

12 Y. B. Kim, H. Y. Seo, S. H. Kim, T. H. Kim, J. H. Choi, J. S. Cho, Y. C. Kang and G. D. Park, *Small Methods*, 2023, **7**, 2201370.

13 J.-S. Park, S. Y. Yang, J.-K. Lee and Y. C. Kang, *J. Mater. Chem. A*, 2022, **10**, 17790–17800.

14 H. Wang, K. Yu, P. Wang, P. Jia, Y. Yuan and C. Liang, *J. Colloid Interface Sci.*, 2023, **645**, 55–65.

15 Q. Wang, S. Wang, W. Liu, D. Wang, S. Luo, P. Hou, M. Zhou, Y. Zhang, S. Yan and X. Liu, *J. Energy Storage*, 2022, **54**, 105285.

16 M. Yang, Q. Kong, W. Feng, W. Yao and Q. Wang, *Carbon Energy*, 2022, **4**, 45–59.

17 M.-H. Sun, S.-Z. Huang, L.-H. Chen, Y. Li, X.-Y. Yang, Z.-Y. Yuan and B.-L. Su, *Chem. Soc. Rev.*, 2016, **45**, 3479–3563.

18 D. Qiu and Y. Hou, *Green Energy Environ.*, 2023, **8**, 115–140.

19 E. Olsson, J. Cottom, H. Au, Z. Guo, A. C. S. Jensen, H. Alptekin, A. J. Drew, M.-M. Titirici and Q. Cai, *Adv. Funct. Mater.*, 2020, **30**, 1908209.

20 J. Yang, Y. Zhai, X. Zhang, E. Zhang, H. Wang, X. Liu, F. Xu and S. Kaskel, *Adv. Energy Mater.*, 2021, **11**, 2100856.

21 M. Jiang, N. Sun, T. Li, J. Yu, R. A. Somoro, M. Jia and B. Xu, *Small*, 2024, **20**, 2401478.

22 Z. Chen, A. Zhang, C. Geng, J. Xiong, P. Sun, N. Tu, Y. Chen, J. Jiang and Z. Ju, *Mater. Chem. Phys.*, 2023, **303**, 127835.

23 Y. Feng, A. M. Rao, J. Zhou and B. Lu, *Adv. Mater.*, 2023, **35**, 2300886.

24 F. Yuan, C. Shi, Y. Li, J. Wang, D. Zhang, W. Wang, Q. Wang, H. Wang, Z. Li and B. Wang, *Adv. Sci.*, 2023, **10**, 2205234.

25 Z. Liang, S. Gao, Y. Liu, T. Qiu, Y. Shao, R. Qin, J. Cheng, Y. Tang, Y. Wu, J. Shi, F. Pan and R. Zou, *ACS Sustainable Chem. Eng.*, 2022, **10**, 15350–15356.

26 R. Guo, X. Liu, B. Wen, F. Liu, J. Meng, P. Wu, J. Wu, Q. Li and L. Mai, *Nano-Micro Lett.*, 2020, **12**, 148.

27 D. Xu, Q. Cheng, P. Saha, Y. Hu, L. Chen, H. Jiang and C. Li, *Adv. Funct. Mater.*, 2023, **33**, 2211661.

28 C. Chi, Z. Liu, Z. Lu, Y. Meng, C. Huangfu, Y. Yan, Z. Qiu, B. Qi, G. Wang, H. Pang, T. Wei and Z. Fan, *Energy Storage Mater.*, 2023, **54**, 668–679.

29 F. Yuan, S. Zhang, Y. Shao, J. Wang, Z. Li, D. Zhang, H. Sun, Q. Wang, W. Wang, Y. Wu and B. Wang, *Appl. Surf. Sci.*, 2023, **641**, 158491.

30 J. Wang, B. Wang, H. Sun, G. Wang, J. Bai and H. Wang, *Energy Storage Mater.*, 2022, **46**, 394–405.

31 J. Yu, M. Jiang, W. Zhang, G. Li, R. A. Soomro, N. Sun and B. Xu, *Small Methods*, 2023, **7**, 2300708.

32 Y. Fu, Y. Dong, Y. Shen, H. Zhao, G. Shao and Y. Lei, *Small*, 2024, **20**, 2406630.

33 L. Ma, Z. Li, J. Li, Y. Dai, C. Qian, Y. Zhu, H. Wang, K. N. Hui, L. Pan, M. A. Amin, Y. Yamauchi and W. Mai, *J. Mater. Chem. A*, 2021, **9**, 25445–25452.

34 Y. Xu, C. Wang, P. Niu, Z. Li, L. Wei, G. Yao, F. Zheng and Q. Chen, *J. Mater. Chem. A*, 2021, **9**, 16150–16159.

35 W. Wang, T. Bao, H. Wang, X. Jiang, Z.-H. He, K. Wang, Y. Yang, L. Li and Z.-T. Liu, *Mol. Catal.*, 2023, **541**, 113112.

36 Y. Wang, W. Kang, X. Wang, B. Guo, D. Cao, D. Wang and D. Sun, *Nano Mater.*, 2022, **5**, 497–507.

37 X. Bie, K. Kubota, T. Hosaka, K. Chihara and S. Komaba, *J. Mater. Chem. A*, 2017, **5**, 4325–4330.

38 Y. Bai, Y. Dou, L.-H. Xie, W. Rutledge, J.-R. Li and H.-C. Zhou, *Chem. Soc. Rev.*, 2016, **45**, 2327–2367.

39 J. Sun, P. Li, Z. Cheng, C. Tang, A. Du and H. Zhang, *Adv. Funct. Mater.*, 2025, 2500154.

40 M. Li, Y. Wang, Y. Zhang and N. Zhang, *Chem. Eng. J.*, 2025, **506**, 160083.

41 Y. Jiang, N. Xiao, X. Song, J. Xiao, K. Yu, X. Dai, Z. Lv and J. Qiu, *Adv. Funct. Mater.*, 2024, **34**, 2316207.

42 Y. Tian, N. Liu, J. Li, T. A. Otitoju, T. Sun and H. Xue, *J. Alloys Compd.*, 2023, **952**, 169998.

43 X. Huang, J. Gao, Y. Qin, D. Du, R. Liu, Y. Shi, C. Wang, Z. Zhang, J. Zhang, J. Sun, T. Li, L. Yin and R. Wang, *ACS Nano*, 2024, **18**, 21459–21471.

44 Z. Yu, Y. Xie, B. Xie, C. Cao, Z. Zhang, H. Huo, Z. Jiang, Q. Pan, G. Yin and J. Wang, *Energy Storage Mater.*, 2020, **25**, 416–425.

45 Z. Qian, R. Guo, Y. Ma, C. Li, L. Du, Y. Wang, C. Du, H. Huo and G. Yin, *Chem. Eng. Sci.*, 2020, **214**, 115413.

46 W. Feng, N. Feng, W. Liu, Y. Cui, C. Chen, T. Dong, S. Liu, W. Deng, H. Wang and Y. Jin, *Adv. Energy Mater.*, 2021, **11**, 2003215.

47 F. Ma, Z. Li, Z. Zhao, J. Mu, X. Wu, P. Zhou, T. Zhou and J. Zhou, *Energy Storage*, 2024, **102**, 114256.

48 G. Cheng, W. Zhang, W. Wang, H. Wang, Y. Wang, J. Shi, J. Chen, S. Liu, M. Huang and D. Mitlin, *Carbon Energy*, 2022, **4**, 986–1001.

49 M. Qin, C. Chen, B. Zhang, J. Yan and J. Qiu, *Adv. Mater.*, 2024, **36**, 2407570.

50 B. Wang, Z. Zhang, F. Yuan, D. Zhang, Q. Wang, W. Li, Z. Li, Y. A. Wu and W. Wang, *Chem. Eng. J.*, 2022, **428**, 131093.

51 H. Zhang, Z. Chen, Z. Sun, M. Cai, W. Liu, W. Ye, H. Gao, J. Han, Y. Cheng, Q. Zhang and M.-S. Wang, *Adv. Funct. Mater.*, 2023, **33**, 2300769.

52 L. Zhao, S. Sun, J. Lin, L. Zhong, L. Chen, J. Guo, J. Yin, H. N. Alshareef, X. Qiu and W. Zhang, *Nano-Micro Lett.*, 2023, **15**, 41.

53 Y. Zhang, Y. Yang, C. Huang, H. Fan, D. Yuan, W.-B. Luo, A. Hu, Q. Tang and X. Chen, *Electrochim. Acta*, 2021, **394**, 139146.

54 S. Zeng, X. Chen, R. Xu, X. Wu, Y. Feng, H. Zhang, S. Peng and Y. Yu, *Nano Energy*, 2020, **73**, 104807.

55 G. Ding, Y. Xiao, Y. Zhang, Z. Li, L. Wei, G. Yao, H. Niu and F. Zheng, *Inorg. Chem. Front.*, 2022, **9**, 4478–4485.

56 Y. Zhao, Z. Sun, Y. Yi, C. Lu, M. Wang, Z. Xia, X. Lian, Z. Liu and J. Sun, *Nano Res.*, 2021, **14**, 1413–1420.

57 P. Niu, Y. Yang, Z. Li, G. Ding, L. Wei, G. Yao, H. Niu, Y. Min, F. Zheng and Q. Chen, *Nano Res.*, 2022, **15**, 8109–8117.

58 C. Qiu, A. Kumar, D. Qiu, M. Tabish, J. Zhang, Z. Jiang, A. Li, G. Yasin, X. Chen and H. Song, *J. Mater. Chem. A*, 2023, **11**, 22187–22197.

59 J. Wang, Z. Huang, W. Zhang, Q. Li, Z. Liang, J. Lu, Z. Lin, G. Wang, J. Wu and S. Huang, *Adv. Funct. Mater.*, 2024, **34**, 2409937.